

Contents

I	A search for highly ionising, short tracks at the CMS detector	1
1	Motivation	3
2	General search strategy	5
2.1	Comparison to earlier searches	10
3	Improved dE/dx measurement for short tracks	11
3.1	Ionisation loss of charged particles	12
3.2	Energy calibration of the silicon pixel tracker	14
3.3	Discrimination of highly-ionising particles	18
3.4	Discrimination improvements	21

11

Part I

12

A search for highly ionising, short tracks at the CMS detector

13

1 Motivation

Supersymmetry is able to offer solutions to many unexplained phenomena in astrophysics and can solve many of the shortcomings of the Standard Model of particle physics (see Section ??). While SUSY has been analysed at previous particle colliders including Tevatron and LEP [1, 2], the LHC with its high centre-of-mass energy offers a unique opportunity to investigate SUSY models with high particle masses that were not accessible in previous experiments.

Therefore, a variety of searches were hunting for SUSY during the Phase I run at the LHC in 2012. Proton-proton collision data from the CMS and ATLAS experiments were analysed with a strong focus on the search for SUSY in the strong production sector (e.g. [3–5]). As a consequence, wide regions of SUSY parameter space are already excluded. However, due to the unknown mechanism of supersymmetry breaking, the most general parametrisation of Supersymmetry introduces over 100 new parameters and thus opens up an incredibly large phenomenological space. Therefore, SUSY models can lead to a plethora of possible signatures at particle colliders. Such more “exotic” SUSY scenarios include models with compressed spectra, where two or more particles are nearly mass-degenerate.

Especially scenarios with a nearly mass-degenerate lightest chargino ($\tilde{\chi}_1^\pm$) and lightest neutralino ($\tilde{\chi}_1^0$) are very interesting from a theoretical perspective as they can help to explain the sources of the relic density [6–8]. In R-parity conserving Supersymmetry, such a mass-degeneracy naturally occurs in case of wino-like neutralinos and charginos, since the mass gap between W_3 and $W_{1/2}$ is fully determined by higher loop corrections (see Section ??). While it is not possible to explain the full relic density with thermally produced neutralinos for $m_{\tilde{\chi}_1^0} \lesssim 2.9$ TeV [9], neutralinos can still be the dominant part if they are non-thermally produced via the decay of a long-lived particle such as a wino-like chargino. The enhanced annihilation cross section (called Sommerfeld enhancement) into WW -, ZZ - or ff -pairs for a wino-like dark matter candidate leads to an underprediction of the relic density if the neutralino and chargino masses are too small [10]. This underprediction can be cured, however, if there is an additional non-thermal production of dark matter that is caused by the decay of a long-lived chargino.

SUSY scenarios with nearly mass-degenerate particles have two distinctive phenomenological properties that require a very different search strategy compared to general SUSY searches. First, if mother and daughter particles in a two body decay are almost mass-degenerate ($\Delta m \lesssim 200$ MeV), the remaining decay product is very soft in p_T , making it

hard to detect. Second, the mother particle is long-lived due to phase space suppression (see Section ??) and may traverse several detector layers before decaying.

Although supersymmetric models with nearly mass-degenerate $\tilde{\chi}_1^\pm$ and $\tilde{\chi}_1^0$ lead to exotic signatures with long-lived charginos and soft decay products, existing SUSY searches at CMS can in principle be sensitive to these models. The exclusion power of existing SUSY searches can be assessed by interpreting their results in terms of the fraction of excluded parameter points in the phenomenological MSSM (see Section ?? for an introduction to the pMSSM). The results of such a study which has been performed in [11] are shown in Figure 1.1. It can be seen that general SUSY searches (blue area) are sensitive to shorter

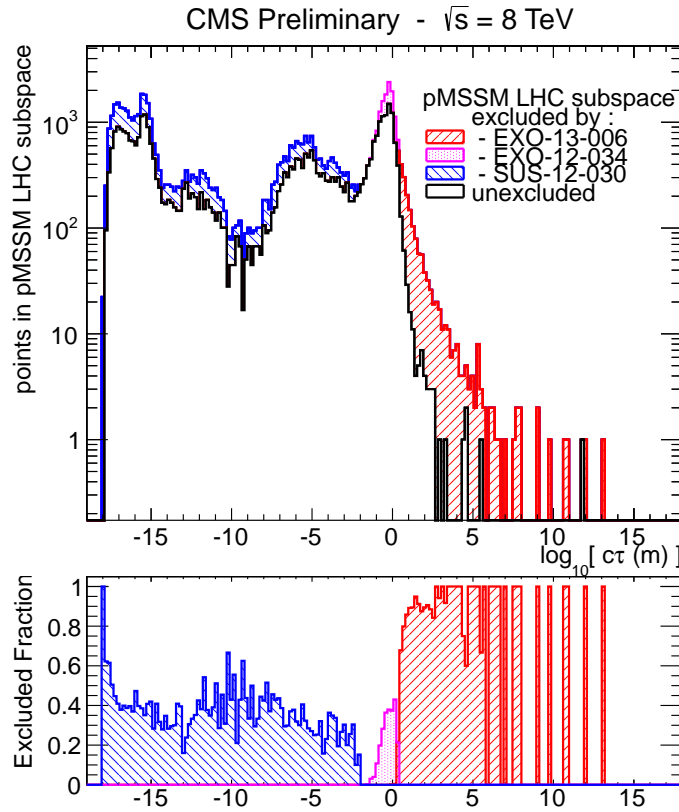


Figure 1.1: The number of excluded pMSSM points at 95% C.L. (upper part) and the fraction of excluded pMSSM points (bottom part) vs. the chargino lifetime for different CMS searches. Red area: the search for long-lived charged particles [12], Purple area: the search for disappearing tracks [11], Blue area: a collection of various general SUSY searches [13] The black line indicates the unexcluded pMSSM parameter points. The sampling of the parameter space points was done according to a prior probability density function which takes pre-LHC data and results from indirect SUSY searches into account (see [14] for further details). Taken from: [15].

chargino lifetimes ($c\tau \lesssim 10$ cm). Due to technical reasons¹, the general SUSY searches were never interpreted in the context of SUSY models with longer chargino lifetimes. Two existing searches, the search for long-lived charged particles [12] and the search for disappearing tracks [11] focus on long and intermediate chargino lifetimes, respectively. These two searches (purple and red areas) are sensitive to chargino lifetimes of $c\tau \gtrsim 35$ cm. Taken together, the existing searches exclude a large fraction of pMSSM points at different chargino lifetimes. However, there is a gap between the general SUSY searches and the search for disappearing tracks that is not accessible by any of the existing searches.

The here presented analysis aims at targeting this gap by optimising the search strategy for charginos with intermediate lifetimes of $10 \text{ cm} \lesssim c\tau \lesssim 40 \text{ cm}$. It is the first analysis at CMS focusing on two signature properties that are highly distinctive for charginos with intermediate lifetimes: first, the characteristically high ionisation losses of heavy charginos; second, short reconstructed tracks due to chargino decays early in the detector.

The associated challenges and the general search strategy of this analysis will be presented in the next section.

2 General search strategy

At the LHC, there are several possible chargino production channels. Chargino pairs can be produced through a photon or a Z -boson exchange. The chargino then decays via a virtual W -boson to the lightest neutralino and a fermion pair (e.g. a pion). This process is illustrated in the Feynman diagram in Fig. 2.1. Other possible chargino pair production channels include the exchange of a supersymmetric Higgs boson or a t -channel squark exchange (Fig. 2.2).

Apart from pair production, charginos can be produced via the chargino neutralino production channel. On tree-level, there exist two production mechanisms: the s -channel W -boson exchange and the t -channel squark exchange (Fig. 2.3).

Alternatively, charginos can be produced via strong production modes, i.e. in cascade decays of new heavy particles, such as gluinos or squarks. In those cascade decays, other particles are additionally produced and lead therefore to different signatures in the detector. Thus, these strong production channels won't be considered in this analysis since they would require other optimised search strategies.

¹The pMSSM interpretation relied on the use of fast simulation techniques which are not capable of simulating charginos with lifetimes $c\tau > 1$ cm.

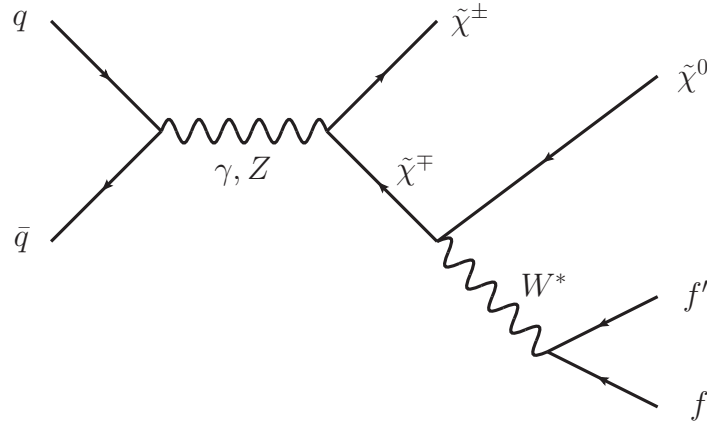


Figure 2.1: Feynman diagram of chargino pair production via gamma or Z -boson exchange and the subsequent decay via a virtual W -boson.

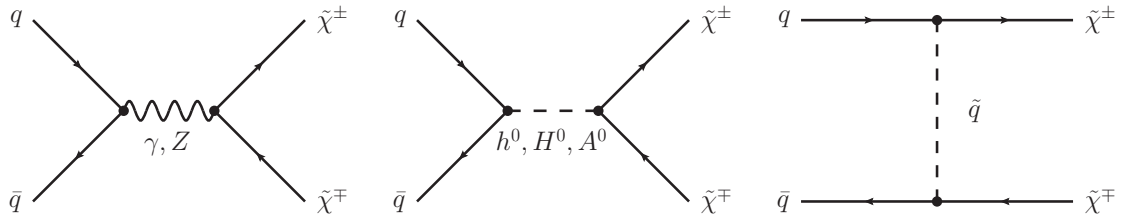


Figure 2.2: Main tree-level diagrams for chargino pair production.

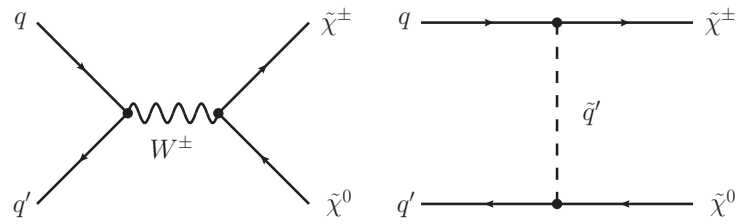


Figure 2.3: Main tree-level diagrams for chargino neutralino production.

When searching for supersymmetric models with long-lived $\tilde{\chi}_1^\pm$, the strategy is of course highly dependent on the actual lifetime of the chargino. For long lifetimes, the chargino can reach the muon chambers and can be reconstructed as a muon even despite a longer time-of-flight [16]. For lower lifetimes, the chargino can already decay inside the detector (e.g. the tracker), and can hence not be reconstructed as a muon but leads to an isolated, potentially disappearing track in the tracker. The detector signatures of these two scenarios are visualised in Fig. 2.4, where simulated chargino-chargino events are shown in a cross-sectional view of the CMS detector. In the left picture of Fig. 2.4, both charginos are reconstructed as muons, which can be seen in the energy deposition in the muon chambers. In the middle and right pictures both charginos have a lower lifetime of $c\tau = 0.5$ m and thus are only visible as tracks in the tracker, where both trajectories end inside the silicon strip tracker. Since this analysis targets a search for Supersymmetry with charginos of lifetimes between $c\tau \approx 10$ cm – 40 cm, the charginos decay rather early in the detector, even in the inner layers of the tracker. Thus, the signature of chargino events consists of isolated, short tracks and the signatures of the decay products, i.e. of a neutralino and a fermion pair.

In case of R-parity conservation one of the chargino decay products, the neutralino, is stable and weakly interacting, thus traversing the detector without leaving any further signature. The missing transverse energy of the neutralino is balanced by the missing transverse energy of the second produced SUSY particle. This is either a neutralino or

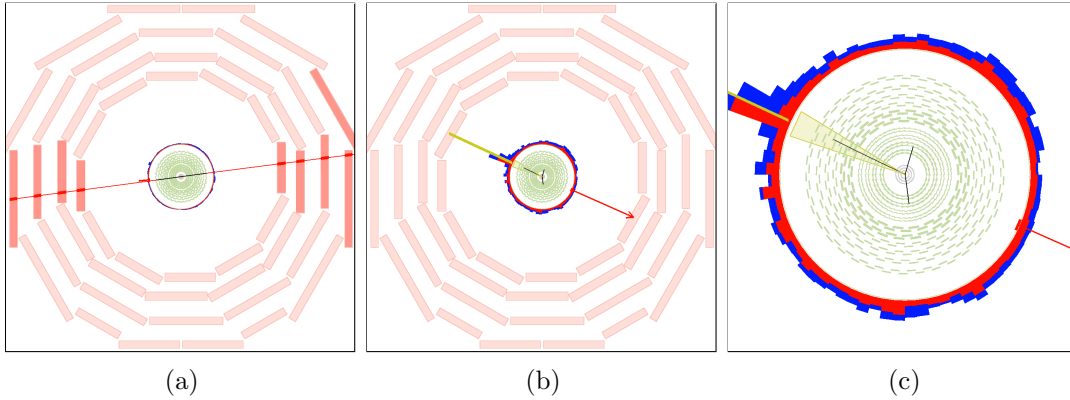


Figure 2.4: Visualisation of possible signatures of a chargino pair produced with a lifetime of $c\tau = 10$ m (a) and a lifetime of $c\tau = 0.5$ m (b and c). The muon chambers are the outer layers of the detector and are depicted as red boxes. The black lines represent the reconstructed chargino tracks. The right picture is a zoom of the picture in the middle. Here, only the cross-section of the tracker (green wavy lines for the strip and grey lines for the pixel) is displayed. The red arrow shows the missing transverse energy in the event. The red (blue) towers correspond to the energy deposition in the ECAL (HCAL).

the decay products of the chargino in events with chargino pairs.

The signature of the other decay product, the fermion pair, can in principle be used to select chargino events. However, for mass-degenerate charginos, it can be very hard or even impossible to detect these fermions as will be explained in detail in the next paragraph.

First of all, the fermionic decay product (e.g. a pion) can usually not be reconstructed because it does not origin from the primary vertex. Secondly, it is very low in momentum because of the mass-degeneracy between $\tilde{\chi}_1^\pm$ and $\tilde{\chi}_1^0$. The typical momentum of a pion originating from a chargino to neutralino decay in the $\tilde{\chi}_1^\pm$ rest frame is of the order

$$p_\pi \sim \sqrt{m_{\tilde{\chi}_1^\pm} - m_{\tilde{\chi}_1^0} - m_\pi}. \quad (2.1)$$

For a mass gap between $\tilde{\chi}_1^\pm$ and $\tilde{\chi}_1^0$ of $\Delta m = 150$ MeV, the pt distribution of the resulting pion peaks at ~ 100 MeV and ends at $p_T \sim 400$ MeV (Fig. 2.5).

If the transverse momentum of a particle is very low, the particle trajectory is much more bended compared to a particle with higher p_T (see Fig. 2.6 for illustration). Due to this bending, the track reconstruction efficiency of particles with a transverse momentum below 1 GeV decreases rapidly, reaching around 40% for isolated pions with a p_T of 100 MeV produced in the primary vertex [17]. It is therefore impossible to rely on a reconstruction of the fermionic chargino decay products in this analysis.

In summary, the signature of chargino events in mass-degenerate SUSY models consists only of a - potentially - disappearing track. Such a signature is very difficult to detect, especially since CMS doesn't offer a dedicated track trigger so that triggering on the

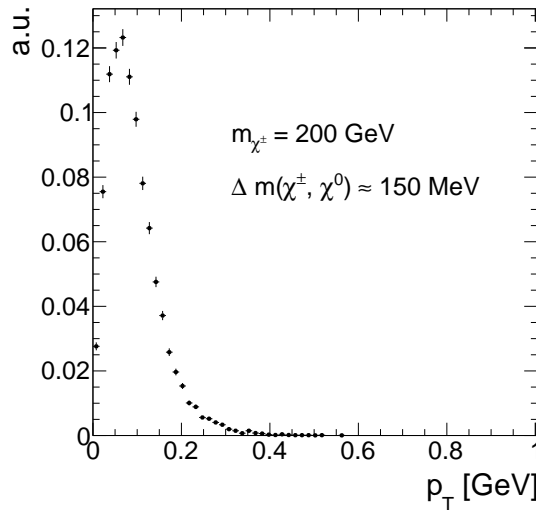


Figure 2.5: Transverse momentum distribution of pions coming from chargino decay into a neutralino with a mass gap of 150 MeV.

chargino track is impossible.

In order to search for such signatures, one therefore needs to trigger on other, less obvious properties of chargino events. This analysis takes advantage of higher order contributions to the Feynman diagrams shown in Figs. 2.2 and 2.3, resulting in initial state radiation (ISR). If the initial quarks radiate a high p_T gluon, the resulting jet can be detected and can offer a possibility to search for events with nothing more than isolated tracks. Furthermore, the non-detection of the chargino's decay products plus a high p_T ISR jet lead to missing transverse energy (MET) in the event. Exploiting these two circumstances, it is possible to detect chargino-pair or chargino-neutralino events with the help of Jet+MET triggers.

Since Jet+MET triggers are not very specific for chargino events, it is important to identify further track properties that can be used to select chargino candidates. One distinctive property of charginos compared to SM particles is their high mass. Therefore, charginos can be identified by selecting high p_T tracks. Furthermore, the energy loss per path length (dE/dx) depends quadratically on the particle's mass for low velocities ($0.2 < \beta\gamma < 0.9$):

$$\left\langle \frac{dE}{dx} \right\rangle = K \frac{m^2}{p^2} + C$$

Therefore, dE/dx constitutes a very nice discriminating variable for massive particles like charginos against SM particles. The selection of chargino events in this analysis thus relies on the selection of isolated high p_T tracks with high dE/dx values.

If the chargino decays before it has crossed the full pixel and strip detector, the associated track is disappearing. For low lifetimes, the tracks can be very short and can

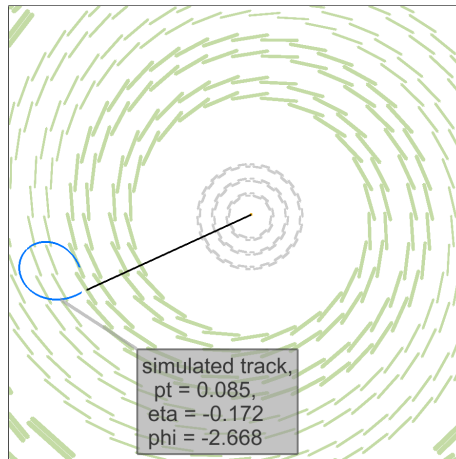


Figure 2.6: Cross-sectional view of the tracker (silicon strip (silicon pixel) tracker layers are illustrated with green (grey) lines) and a simulated chargino track (black line) decaying to a pion (bended blue line) with a p_T of ~ 85 MeV and a neutralino (not visible).

have only a few hits in the detector. In order to reconstruct a particle's trajectory, a minimum of three hits are required since defining a helical path requires five parameters (see [17]). A specific challenge for this analysis is hence the combination of searching for short tracks and utilising the measurement of the energy deposition of the chargino. For very short tracks, eventually only passing the first couple of layers of the whole tracker system, the pixel tracker information becomes very important. Therefore, an accurate energy measurement in the pixel system is of great importance to this analysis. However, no other CMS analysis has used the energy information of the pixel tracker so far. This analysis thus requires a thorough study of the quality of the pixel energy calibration and, potentially, a recalibration in case the pixel energy calibration is not sufficient.

2.1 Comparison to earlier searches

As already mentioned before, there are two analyses at CMS at $\sqrt{s} = 8$ TeV with 20 fb^{-1} data that search for intermediate lifetime charginos, the search for long-lived charged particles [12] and the search for disappearing tracks [11]. The here presented analysis aims at achieving an increase in sensitivity towards shorter lifetimes compared to the earlier analyses in a twofold way. First, the selection is optimised for the inclusion of very short tracks. Second, the inclusion of the variable dE/dx is used to increase the search sensitivity compared to [11].

In [12], a minimum number of eight hits were required for every track, whereas [11] required a minimum of seven hits. This can be very inefficient for shorter lifetimes, where most of the charginos already decay shortly after the pixel tracker. In Fig. 2.7 (left), the normalised distribution of the number of measurements (N_{hits}) of chargino tracks is shown. It can be seen, that N_{hits} peaks at the minimal possible value needed for track reconstruction of $N_{\text{hits}} = 3$ for lower lifetimes. For a lifetime of $c\tau = 50\text{ cm}$, a second peak at ~ 17 hits appears corresponding to the number of measurements when crossing all pixel barrel (3) and strip inner and outer barrel (6 from stereo and 8 from normal) layers. However, a notable fraction of $\sim 40\%$ of chargino tracks still has a number of measurements of $N_{\text{hits}} < 8$.

It should be also mentioned, that the track reconstruction efficiency is sufficient for short chargino tracks, such that a loosening of the N_{hits} requirement is expected to be really improving the signal acceptance. The track reconstruction efficiency for different chargino decay points is depicted in Fig. 2.7 (right). For very short tracks ($N_{\text{hits}} = 3$) the efficiency is still around 20%.

Additionally, the search for disappearing tracks which targets models with charginos decaying inside the tracker did not make use of the high energy deposition of heavy parti-

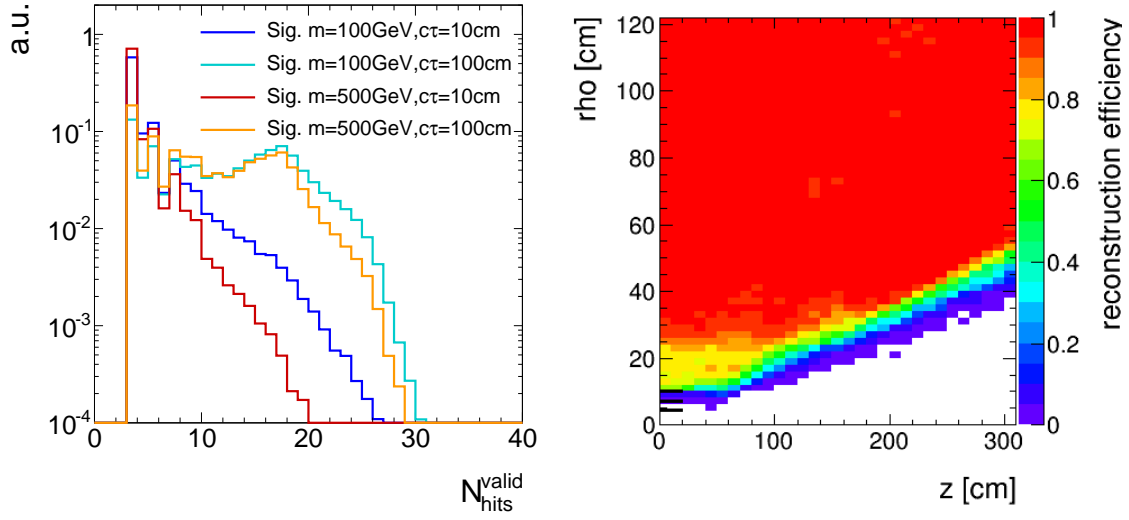


Figure 2.7: Left: Number of measurements in the tracker system N_{hits} for four different signal lifetimes. Right: Probability to reconstruct a track (z) in dependency of the chargino's decay point (x and y). More information on the generation of the simulated signal samples can be found in Section ??.

cles. Although this variable was indeed used in the search for long-lived charged particles, this search was not optimised for intermediate lifetimes (e.g. no explicit muon veto on the selected tracks was required). Thus, it shows less sensitivity compared to the disappearing track search in the lifetime region between $35\text{ cm} \lesssim c\tau \lesssim 100\text{ cm}$ (see Fig. 1.1).

To conclude, the general search strategy of the here presented analysis is to unite the strategies of [12] and [11] and to lower the strong selection on the number of hits in these analyses in order to get an optimised selection for lifetimes around $10\text{ cm} \lesssim c\tau \lesssim 40\text{ cm}$.

3 Improved dE/dx measurement for short tracks

As already pointed out in the previous chapter the inclusion of the pixel energy measurements can increase the sensitivity when searching for short and highly ionising tracks. While the silicon strip detector has already been calibrated as part of the search for long-lived charged particles [12], no complete calibration has been done for the pixel silicon tracker so far. To increase the discrimination power of dE/dx for short tracks, such a calibration procedure is therefore conducted within this PHD thesis.

The CMS tracker system provides a measurement of a particle's energy loss for each hit in the tracker. This is done by the detection of the number of electrons produced by the ionisation of the silicon. A detailed introduction to the CMS tracker system and the energy measurement can be found in Section ??.

How to combine the single energy measurements for each tracker hit into one track dE/dx estimator that can be used for analysis purposes will be explained in the following Section 3.1. The pixel energy calibration is then described in Section 3.2. How to discriminate SM particles and beyond SM particles with the help of a dE/dx measurement is discussed in Section 3.3, followed by the exploration of the achieved discrimination improvements in Section 3.4.

3.1 Ionisation loss of charged particles

Energy losses for moderately relativistic charged particles travelling through matter are mostly caused by ionisation effects. The mean energy loss per path length can be described with the Bethe formula [18]:

$$\langle \frac{dE}{dx} \rangle = K z^2 \frac{Z}{A} \frac{1}{\beta^2} \left[\frac{1}{2} \ln \frac{2m_e c^2 \beta^2 \gamma^2 T_{\max}}{I^2} - \beta^2 - \frac{\delta(\beta\gamma)}{2} \right]. \quad (3.1)$$

It is a function of the atomic number (Z), the atomic mass (A) of the absorber, and the mean excitation energy (I) which is 173 eV [19] for silicon. T_{\max} represents the maximum energy transfer in a single collision. The relevant particle's properties are the velocity (β), the Lorentz factor (γ) and the charge (z) of the incident particle. The density correction $\delta(\beta\gamma)$ reduces the mean energy loss at high energies because of polarisation effects of the material. The factor K is constant and is 0.307 in units of $\text{MeV mol}^{-1} \text{cm}^2$. The Bethe formula is valid if the main energy loss originates from ionisation effects, i.e. in a region between $0.1 \lesssim \beta\gamma \lesssim 1000$.

Even if widely used, the mean energy loss is a quantity which is “ill-defined experimentally and is not useful for describing energy loss by single particles” [20]. The problem is caused by the underlying probability distribution of one single dE/dx measurement (this will be named $\Delta E/\Delta x$ throughout the following sections), which can be parametrised by a Landau distribution [21]

$$p(x) = \frac{1}{\pi} \int_0^\infty e^{-t \log t - xt} \sin(\pi t) dt. \quad (3.2)$$

The Landau distribution has no free parameters. Its most probable value is around 0.222. However, it is possible to introduce artificially a different most probable value and a width (at half maximum) with $x \rightarrow \frac{x - \text{MPV}}{\sigma} - 0.222$. The Landau distribution is a highly asymmetric distribution with a long tail towards the right end (see Fig. 3.1). Theoretically

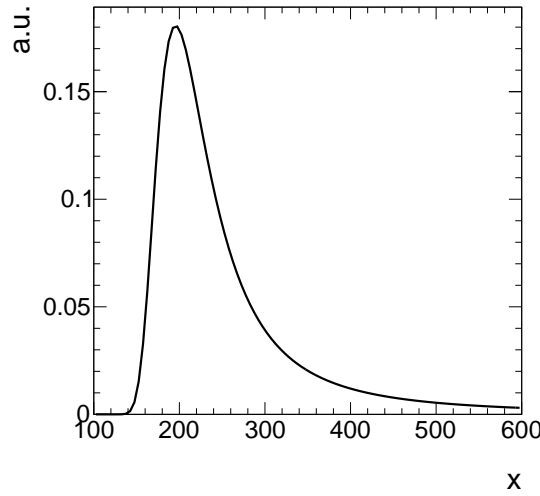


Figure 3.1: Illustration of the shape of a Landau distribution. Parameters were chosen as $\mu = 200$ and $\sigma = 20$.

it extends to infinite energies, however in nature the maximal deposited energy is of course limited by the particle's full energy. Because of its strong asymmetry, measurements of the mean energy loss per path length $\langle dE/dx \rangle$ with only a few single measurements are easily biased towards high values, making the mean energy loss described by the Bethe formula a problematic and unstable concept.

A much better observable is the most probable value (MPV) of the Landau distribution. The MPV is much more stable compared to the mean and is not as easily biased towards higher dE/dx values. The most probable energy loss of a charged particle, Δ_p , can be described by the Landau-Vavilov-Bichsel equation [22]:

$$\Delta_p = \xi \left[\ln \frac{2m_e c^2 \beta^2 \gamma^2}{I} + \ln \frac{\xi}{I} + j - \beta^2 - \delta(\beta\gamma) \right], \quad (3.3)$$

with $\xi = (K/Z)\langle Z/A \rangle(x/\beta^2)$. The thickness of the absorber x appears explicitly in the Landau-Vavilov-Bichsel equation making the most probable energy loss per path length Δ_p/dx logarithmically dependent on x . A comparison between the Bethe mean energy loss $\langle dE/dx \rangle$ and the most probable energy loss Δ_p/dx is shown in Fig. 3.2.

In order to estimate experimentally the most probable dE/dx value from only a few energy measurements, several “estimators” can be used that suppress a potential bias towards the high end without introducing a bias towards lower values [23]. One of the

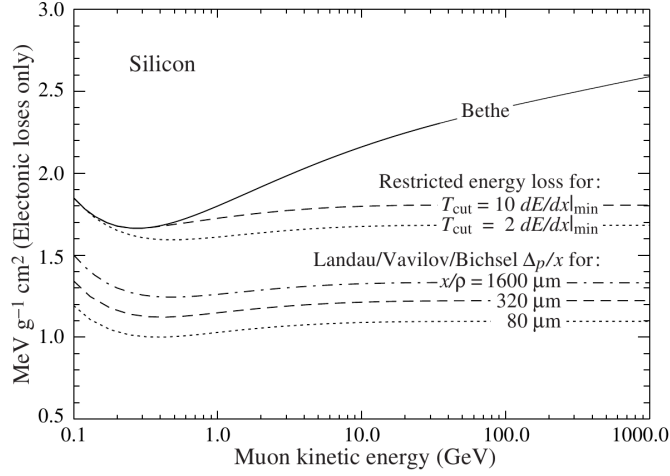


Figure 3.2: Comparison between the Bethe mean energy loss, restricted energy loss and the most probable energy loss described by the Landau-Vavilov-Bichsel function for muons for different values of absorber thickness. Taken from [20].

estimators for determining a tracks's dE/dx is the harmonic-2 estimator

$$I_{h2} = \left(\frac{1}{N} \sum_{i=1}^N (\Delta E_i / \Delta x_i)^{-2} \right)^{-1/2}, \quad (3.4)$$

where $\Delta E_i / \Delta x_i$ corresponds to the ΔE and Δx measurement in the i th hit of the track. The harmonic mean of all N measurements to the power of two is used as estimator for the MPV of the dE/dx distribution of a particle.

The harmonic-2 estimator is also used for the pixel energy calibration described in the following section.

3.2 Energy calibration of the silicon pixel tracker

During Run I in 2012, the pixel silicon detector was continuously subjected to an energy calibration, a so-called gain calibration. Every pixel was calibrated to the same response, so that the whole pixel tracker should have been well inter-calibrated [24]. Unfortunately, due to various reasons, such as the imperfect constancy of the reference signal, or radiation and temperature induced changes, the energy calibration could not ensure a fully calibrated pixel tracker. This imperfection of the gain calibration can be seen in Fig. 3.3, where the sum of the harmonic-2 estimator for all tracks $\sum_{\text{all trks}} I_{h2}$ over the full data-taking period in 2012 is shown. Four different steps can be spotted. The first and the third steps correspond to changes in the settings of the tracker due to irradiation. The second and fourth step are induced by associated adjustments in the online gain calibration. Unfortunately, although

the gain calibration was adjusted (even with some delay), it was not able to ensure a constant energy response of the pixel tracker over time. The variations of the dE/dx measurement over time of around 15% are too large to use dE/dx without a further calibration.

The following sections explain the method of the gain calibration of the pixel silicon tracker which is conducted for this analysis. It is splitted into a section about the inter-calibration of gain and the absolute calibration of gain. Detailed technical information about the pixel tracker can be found in Section ??.

Inter-calibration of gain

The main goal of the gain calibration is to get a uniform response in the ionisation energy loss dE/dx over the full data taking period in 2012. To also ensure a uniform response of all modules within one time step, an additional inter-calibration on module level is carried out. The inter-calibration can in principle be done on various levels: the highest granularity would be a calibration on pixel level, followed by a calibration on read-out-chip (ROC) level and then on module-level. Lower granularities in descending order are rings (modules with same z-position) and finally layers (3 layers in the barrel and 4 disks in the endcap). It is checked that all pixels and all ROCs (on one module) are well inter-calibrated, such that the inter-calibration is finally done module-wise.

The gain calibration of the pixel silicon tracker is carried out with the help of minimally ionising particles (MIPs). MIPs in this context are not defined as particles depositing a minimum amount of energy, but more generally a small amount of energy. This denotes

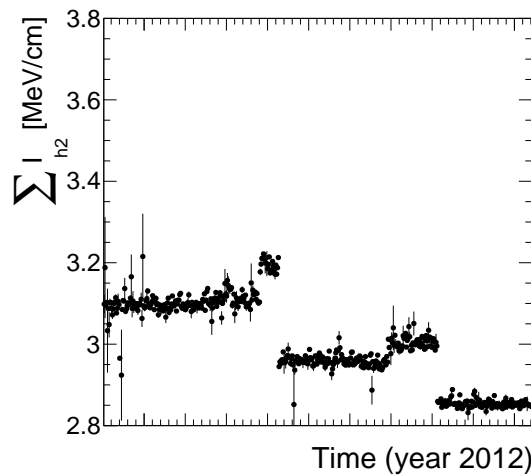


Figure 3.3: Sum of all track's dE/dx (harmonic-2 estimator) over the full year 2012. Only pixel hits are taken into account. Every data point corresponds to one run.

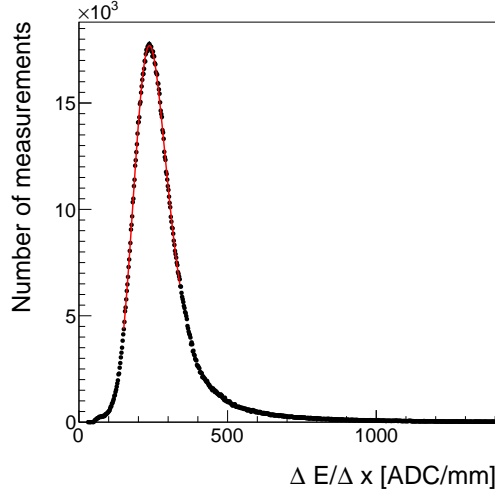


Figure 3.4: An example of the $\Delta E/\Delta x$ distribution measured in ADC count per mm for one module of the CMS pixel tracker. A Landau convoluted with a Gaussian is fitted to the core of the distribution in an iterative procedure.

all particles located at the plateau of the dE/dx distribution vs. momentum (see Fig. ??). This approach ensures that all particles deposit similar amount of energy so that the variation due to different momenta is minimised. MIPs are selected by a momentum selection of $p > 2$ GeV. Additionally, only tracks with at least eight hits and a $\chi^2/\text{n.d.o.f.} < 3$ are used to ensure a high-quality track reconstruction. A sample containing around 50 million “minimum bias” events is used for calibration. The “minimum bias” sample was specifically recorded for tracker calibration purposes. Its distinctive property is that neither an online nor offline selection was applied.

For every module in the pixel tracker (there are 1440 modules in total), a distribution of the energy loss per path length $\Delta E/\Delta x$ is built. The measurement of $\Delta E/\Delta x$ is done in ADC counts per mm. ADC counts are a measure for the deposited charge after digitisation. Figure 3.4 shows an example distribution for one module. The underlying Landau distribution can be nicely seen. To extract the MPV for every module a fit to the core distribution is performed. The fit is done with a Landau convoluted with a Gaussian function to be closer to the experimentally observed energy spectrum. This also increases the fit performance and the stability of the fit. The path length Δx is calculated with

$$\Delta x = d_{\text{module}_i} \cdot \cos(\phi_{\text{track}}),$$

where d_{module_i} is the thickness of module i and ϕ_{track} is the relative angle of the particle’s trajectory to the normal axis of the module. With the measured MPV extracted from the

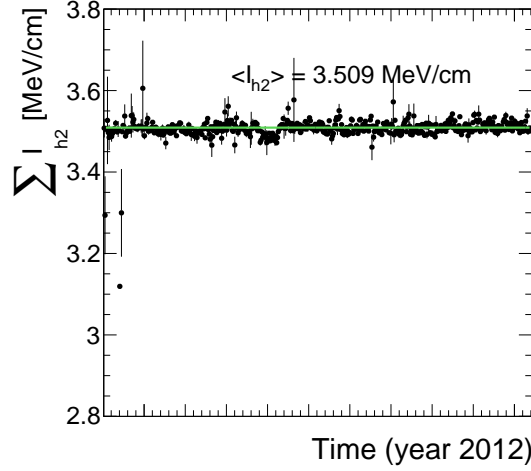


Figure 3.5: Sum of all track's dE/dx (harmonic-2 estimator) over the full year 2012 after applying the calibration factors, resulting in an average dE/dx of 3.51 MeV/cm. Only pixel hits are taken into account. Every data point corresponds to one run.

fit, an inter-calibration factor is calculated for every module

$$c_{\text{inter}} = \frac{\text{MPV}_{\text{target}} [\text{ADC/mm}]}{\text{MPV} [\text{ADC/mm}]} = \frac{300 \cdot 265 \text{ ADC/mm}}{\text{MPV} [\text{ADC/mm}]}.$$

The factor $300 \cdot 265 \text{ ADC/mm}$ is in principal an arbitrary number since the final response is adjusted by the absolute gain calibration described in the next section. However, it is chosen such that it corresponds approximately to the most probable energy deposition of a MIP. The calibration factor can then be used to scale every single measurement in a module to a calibrated $\Delta E/\Delta x$ measurement

$$\frac{\Delta E}{\Delta x}_{\text{calibrated}} = c_{\text{inter}} \cdot \frac{\Delta E}{\Delta x}_{\text{uncalibrated}}$$

The determination of the calibration factor needs to be done for every of the five time steps, shown in Fig. 3.3 independently, in order to get rid of the time dependency. The result of the inter-calibration can be seen in Fig. 3.5. The variation over time is indeed eradicated, resulting in a maximal time variation of less than $\sim 1\%$.

Additionally, the same procedure is carried out for a corresponding simulated data sample to ensure the inter-calibration of the pixel modules on all simulated samples.

Absolute calibration of gain

As a final step, the targeted MPV being $\text{MPV}_{\text{target}} = 300 \cdot 265 \text{ ADC/mm}$ needs to be translated to a meaningful physical quantity given in physical units (e.g. MeV/cm). That means, that the charge measurement in ADC counts needs to be converted to the real energy release of a particle. The relation between ΔE in ADC counts and the energy loss in eV is given by

$$\Delta E [\text{eV}] = c_{\text{inter}} \cdot \Delta E [\text{ADC}] \cdot \frac{N_e}{\text{ADC}} \cdot 3.61 \text{ eV},$$

where N_e/ADC is the number of electrons which correspond to one ADC count and 3.61 eV is the mean energy needed to create one electron-hole pair in silicon at -10°C. Such an absolute gain calibration can be done with the help of several methods (all explained in [23]). The absolute calibration of the silicon pixel tracker can rely on the already conducted absolute calibration of the silicon strip detector. In [23], the absolute gain calibration was done with the help of the most probable energy release per path length of muons, theoretically described by the Landau-Vavilov-Bichsel formula in Eq. (3.3). To calibrate the pixel tracker to the correct energy loss per path length it is therefore sufficient to determine one calibration factor to relate the average dE/dx of all tracks in the pixel tracker as shown in Fig. 3.5 to the average measured dE/dx in the strip tracker, shown in Fig. 3.6 by

$$c_{\text{absolute}} = \frac{dE/dx_{\text{strip}}}{dE/dx_{\text{pixel}}} = \frac{3.303}{3.509} = 0.941.$$

This factor is then applied on top of c_{inter} for all pixel modules.

Finally, an absolute calibration factor needs to be determined for the simulated samples, where the simulated pixel tracker is calibrated to the average dE/dx of the silicon strip measured in data.

3.3 Discrimination of highly-ionising particles

As mentioned before, it is difficult to find a robust estimator for the MPV of the Landau distribution, if only a few single measurements of $\Delta E/\Delta x$ are available. The harmonic-2 estimator I_{h2} was already introduced in Section 3.1 in Eq. (3.4). It is known to be a robust estimator not easily biased by large fluctuation in $\Delta E/\Delta x$ because of the suppression by a factor of two. However, it was shown in [23] that a better discrimination between SM particles and possible new heavy particles can be achieved when using likelihood techniques, i.e. determining the probability that the set of all $\Delta E/\Delta x$ belonging to one track is actually compatible with the hypothetical probability distribution of a MIP.

Testing that a measured sample has been drawn from a specific distribution is known as the Smirnov-Cramér-von Mises test [25, 26], which is deduced from the integral of the

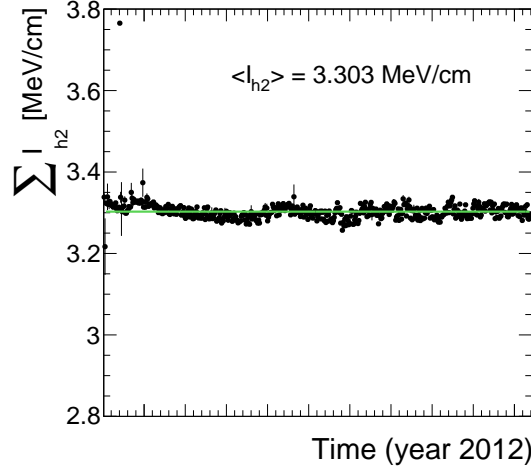


Figure 3.6: Sum of all track's dE/dx (harmonic-2 estimator) measured in the silicon strip detector over the full year 2012. The average most probable dE/dx is $I_{h2} = 3.303$ MeV/cm. Every data point corresponds to one run.

squared difference of the measured distribution $P_N(x)$ to the hypothesis distribution $P(x)$

$$I_s = \int_{-\infty}^{\infty} [P_N(x) - P(x)]^2 dP(x)$$

leading to a test statistics of

$$I_s = \frac{3}{N} \cdot \left(\frac{1}{12N} + \sum_{i=1}^N \left[P_i - \frac{2i-1}{2N} \right]^2 \right),$$

where N is the total number of energy measurements and P_i is the cumulative probability that a MIP would release a $\Delta E/\Delta x$ equal or smaller than the measured $\Delta E/\Delta x$ with all P_i arranged in increasing order.

However, this test statistics is not sensitive to the sign of the difference between the measured and the theoretical distribution. It can therefore not distinguish between incompatibilities due to variations towards higher or lower energy deposits compared to the hypothesis distribution. Thus it is not suitable for the discrimination between MIPs and heavy new particles by dE/dx . A so-called Asymmetric Smirnov-Cramér-von Mises discriminator was developed in [23] which is only sensitive to incompatibilities to the MIP

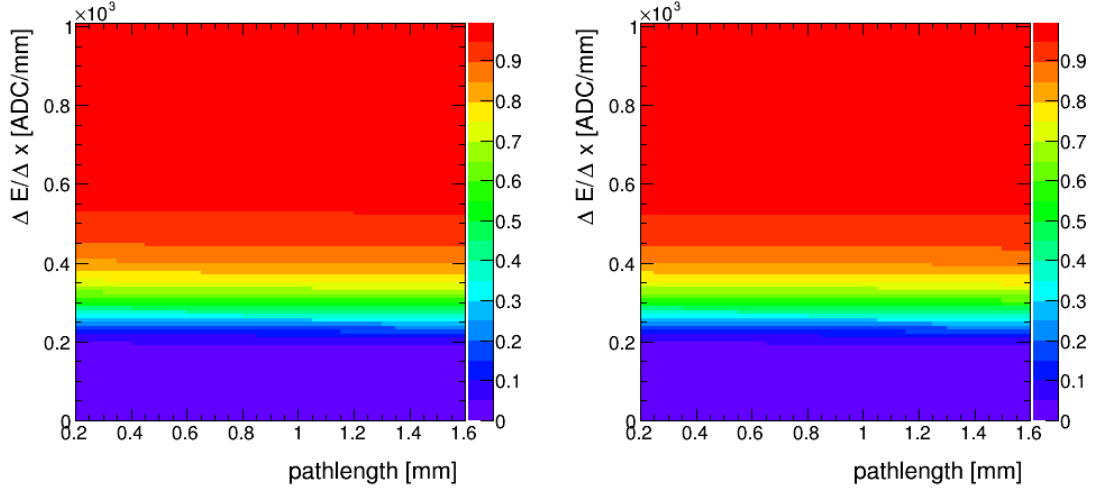


Figure 3.7: Cumulative probability for a MIP to release a $\Delta E/\Delta x$ (y-axis) vs. the path length (x-axis) in data (left) and simulation (right) for the pixel tracker based on the “Minimum bias” sample.

hypothesis towards higher energy depositions

$$I_{\text{as}} = \frac{3}{N} \cdot \left(\frac{1}{12N} + \sum_{i=1}^N \left[P_i \cdot \left(P_i - \frac{2i-1}{2N} \right)^2 \right] \right).$$

A value of I_{as} close to zero indicates good compatibility with the MIP hypothesis, whereas a value close to one indicates worse compatibility because of unexpectedly high energy losses.

The underlying probability P_i of the energy release for a given path length in the pixel tracker is extracted from the same “Minimum bias” sample used for the pixel energy calibration. In total 28 different templates each for a different given path length are created. In Fig. 3.7 the probability distribution template for the pixel tracker in data and simulation is shown. The corresponding templates for the energy release in the silicon strip detector were already built by [23].

A comparison between the energy release by MIPs (I_{as}) in data and simulation for high-quality tracks with $p > 5 \text{ GeV}$ and $|\eta| < 2.1$ can be found in Fig. 3.8.

dE/dx shows good agreement in data and simulation for $I_{\text{as}} < 0.1$. For larger values, I_{as} shows a larger decrease in simulation than in measured data. That’s the reason why a

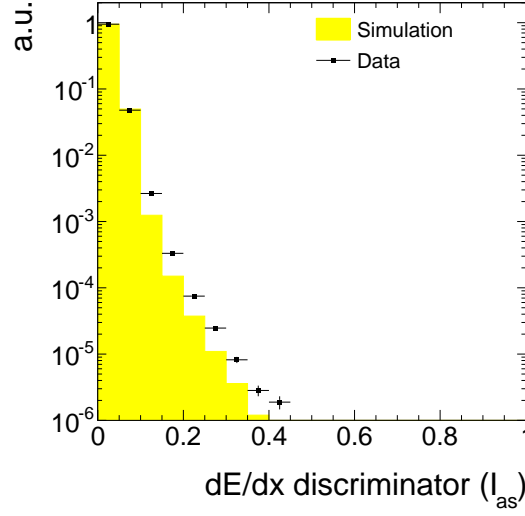


Figure 3.8: Normalised I_{as} distribution for MIPs from the minimum bias sample in data and simulation for high-quality (high purity as defined in [27], a minimum number of eight hits and no missing inner and middle hits) tracks with $p > 5 \text{ GeV}$ and $|\eta| < 2.1$.

data-based approach for analyses exploiting dE/dx information is needed.

3.4 Discrimination improvements

The goal of including the pixel energy information is to increase the discrimination power of I_{as} between background and signal tracks, especially for shorter lifetimes. In Fig. 3.9, a comparison of the shapes of the energy release by MIPs and by signal tracks in simulation is shown (details about the simulated samples can be found in the next section Section ??). It can be seen, that the I_{as} distributions of all signal models show a larger tail towards $I_{\text{as}} = 1$, whereas the I_{as} of the background is rapidly falling. The I_{as} distribution is not only influenced by the velocity (β) of a particle but also by the number of hits of a track. The influence of the velocity can be easily seen in Eq. (3.3). This in turn results in a dependency of I_{as} on the mass of the incident particle. However, also for charginos with same mass, the velocity is higher in average for shorter lifetimes. This is caused by the fact, that for shorter lifetimes (e.g. $c\tau = 10 \text{ cm}$), already a sizable fraction of the charginos decay before reaching the tracker system. The probability of reaching the detector increases for higher velocities because of the boost, which can be clearly seen at the survival probability

$$P(t) = e^{-\frac{t}{\gamma\tau}}. \quad (3.5)$$

389 This means that shorter lifetimes lead to higher average β which in turn lead to lower
 390 values of I_{as} .

391 The number of measurements in the tracker system defines the influence of single fluc-
 392 tuations in $\Delta E/\Delta x$ on the I_{as} discriminator, because of the long right tail of the Landau
 393 distribution, A low number of hits lead therefore to higher I_{as} values.

394 Thus, I_{as} for charginos with lower lifetimes are affected by two things: First, due to
 395 the smaller number of measurements the chargino tends to higher I_{as} values. Second, low
 396 lifetimes charginos have in average a higher velocity leading to lower I_{as} values. Both
 397 effects can be seen in Fig. 3.9 (right). The large tail for longer lifetimes is caused by the
 398 lower velocities, but the small surplus between 0.1 and 0.2 is caused by the smaller number
 399 of measurements for lower lifetimes.

400

401 Finally, the impact of the additional $\Delta E/\Delta x$ information from the pixel tracker on the
 402 selection efficiency of signal and background tracks is quantified. Figure 3.10 shows the
 403 signal selection efficiency against the background selection efficiency for different selection
 404 cuts in I_{as} , once including the pixel information and once without it. The background
 405 selection efficiency is estimated with simulated W +jets events but was additionally checked
 406 on simulated $t\bar{t}$ +jets and QCD-multijet events (further information about the simulated
 407 samples can be found in the next section). No significant difference between these processes

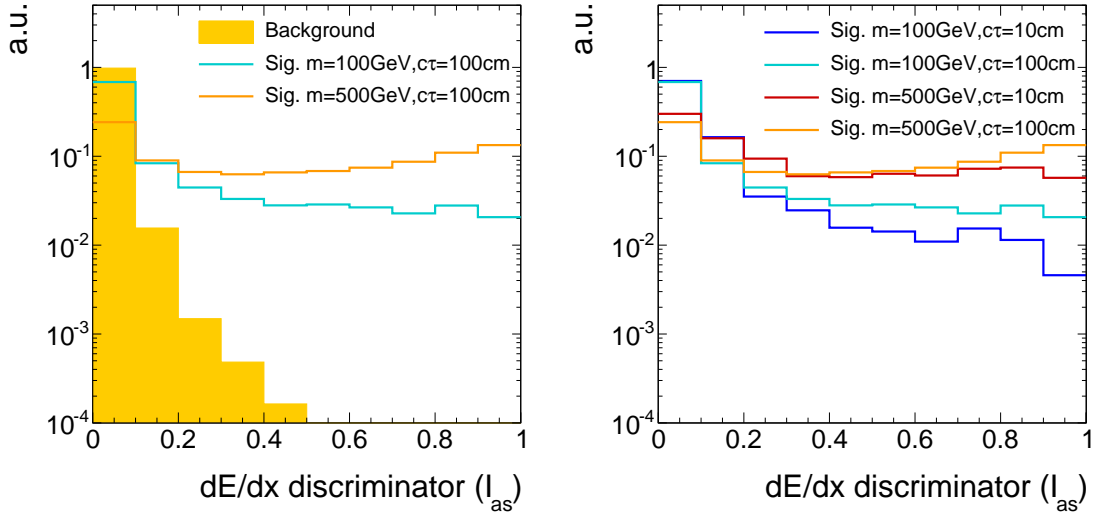


Figure 3.9: Normalised I_{as} distribution for simulated background and signal tracks (left) and for four different signal models (right) for high-purity tracks (as defined in [27]) with $p_{\text{T}} > 10$ GeV and $|\eta| < 2.1$. For the illustration of the background tracks' spectrum simulated $t\bar{t}$ +jets events are used (more information about this sample is given in Section ??).

in the background selection efficiency was observed.

The signal selection efficiency and the background suppression depend on the mass and the lifetime of the charginos. The discrimination power of I_{as} is much better for higher masses as expected.

It can be seen that the inclusion of the pixel information increases the background suppression for a given signal efficiency throughout the investigated signal models. This background suppression improvement is most pronounced for very tight cuts on I_{as} (up to

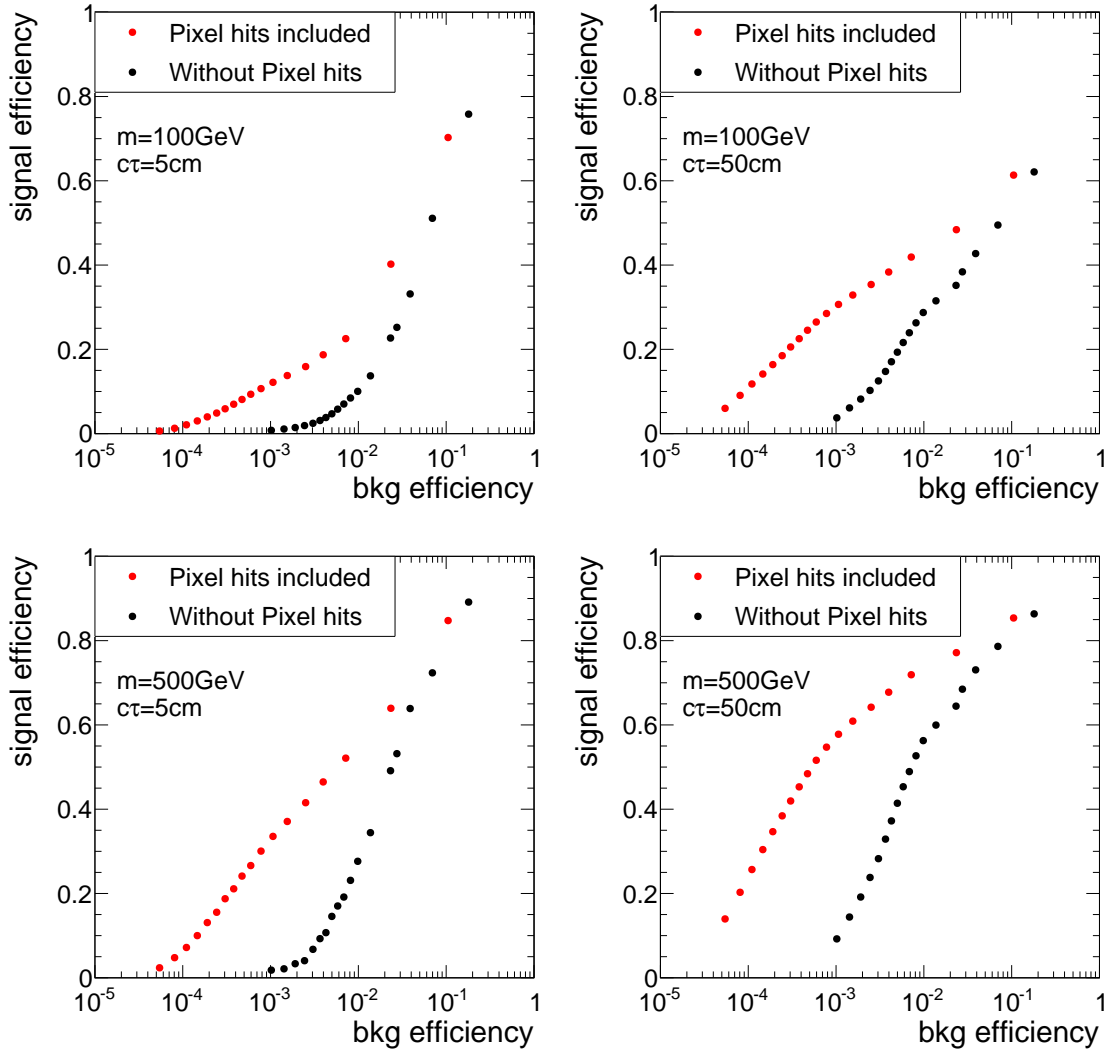


Figure 3.10: Signal selection efficiency vs. background selection efficiency with (red) and without (black) pixel information. Each point correspond to one selection cut in I_{as} . The figure is based on a simulated $W + \text{jets}$ sample and a simulated signal sample with chargino-chargino production, both subject to a selection of high-quality tracks (without a selection on N_{hits}) with $p_{\text{T}} > 10 \text{ GeV}$.

415 a factor of 20) and still considerable for looser selections with signal efficiencies of around
416 40% (factor of 10).

Bibliography

- [1] CDF, D0 Collaboration, T. Adams, “SUSY Searches at the Tevatron”, in *Hadron collider physics. Proceedings, 19th Symposium, HCP2008, Galena, USA, May 27-31, 2008*. 2008. [arXiv:0808.0728](#).
- [2] ALEPH, DELPHI, L3 and OPAL Collaborations, “Joint SUSY Working Group”. <http://http://lepsusy.web.cern.ch/lepsusy/>. LEPSUSYWG (June 2004).
- [3] CMS Collaboration, “Search for new physics in the multijet and missing transverse momentum final state in proton-proton collisions at $\sqrt{s}=8$ TeV”, *JHEP* **06** (2014) 055, [arXiv:1402.4770](#). doi:10.1007/JHEP06(2014)055.
- [4] CMS Collaboration, “Searches for Supersymmetry using the M_{T2} Variable in Hadronic Events Produced in pp Collisions at 8 TeV”, *JHEP* **05** (2015) 078, [arXiv:1502.04358](#). doi:10.1007/JHEP05(2015)078.
- [5] ATLAS Collaboration, “Search for squarks and gluinos with the ATLAS detector in final states with jets and missing transverse momentum using $\sqrt{s}=8$ TeV proton-proton collision data”, *JHEP* **09** (2014) 176, [arXiv:1405.7875](#). doi:10.1007/JHEP09(2014)176.
- [6] T. Moroi and L. Randall, “Wino cold dark matter from anomaly mediated SUSY breaking”, *Nucl. Phys.* **B570** (2000) 455–472, [arXiv:hep-ph/9906527](#). doi:10.1016/S0550-3213(99)00748-8.
- [7] J. Hisano, S. Matsumoto, M. M. Nojiri et al., “Direct detection of the Wino and Higgsino-like neutralino dark matters at one-loop level”, *Phys. Rev.* **D71** (2005) 015007, [arXiv:hep-ph/0407168](#). doi:10.1103/PhysRevD.71.015007.
- [8] M. Ibe, S. Matsumoto, S. Shirai et al., “Wino Dark Matter in light of the AMS-02 2015 Data”, *Phys. Rev.* **D91** (2015), no. 11, 111701, [arXiv:1504.05554](#). doi:10.1103/PhysRevD.91.111701.
- [9] T. Moroi, M. Nagai, and M. Takimoto, “Non-Thermal Production of Wino Dark Matter via the Decay of Long-Lived Particles”, *JHEP* **07** (2013) 066, [arXiv:1303.0948](#). doi:10.1007/JHEP07(2013)066.

- [10] J. Hisano, S. Matsumoto, and M. M. Nojiri, “Explosive dark matter annihilation”, *Phys. Rev. Lett.* **92** (2004) 031303, [arXiv:hep-ph/0307216](#).
[doi:10.1103/PhysRevLett.92.031303](#).
- [11] CMS Collaboration, “Search for disappearing tracks in proton-proton collisions at $\sqrt{s} = 8$ TeV”, *JHEP* **01** (2015) 096, [arXiv:1411.6006](#).
[doi:10.1007/JHEP01\(2015\)096](#).
- [12] CMS Collaboration, “Searches for long-lived charged particles in pp collisions at $\sqrt{s}=7$ and 8 TeV”, *JHEP* **07** (2013) 122, [arXiv:1305.0491](#).
[doi:10.1007/JHEP07\(2013\)122](#).
- [13] CMS Collaboration, “Phenomenological MSSM interpretation of the CMS 2011 5fb-1 results”, *CMS Physics Analysis Summary CMS-PAS-SUS-12-030* (2013).
- [14] CMS Collaboration, “Reinterpreting the results of the search for long-lived charged particles in the pMSSM and other BSM scenarios”, *CMS Physics Analysis Summary CMS-PAS-EXO-13-006* (2014).
- [15] CMS Collaboration, “Search for disappearing tracks in proton-proton collisions at $\sqrt{s} = 8$ TeV”, *Public CMS Wiki* (2015).
<https://twiki.cern.ch/twiki/bin/view/CMSPublic/PhysicsResultsEXO12034>, Topic revision: r9.
- [16] CMS Collaboration, “Search for heavy long-lived charged particles in pp collisions at $\sqrt{s} = 7$ TeV”, *Phys. Lett.* **B713** (2012) 408–433, [arXiv:1205.0272](#).
[doi:10.1016/j.physletb.2012.06.023](#).
- [17] CMS Collaboration, “Description and performance of track and primary-vertex reconstruction with the CMS tracker”, *JINST* **9** (2014), no. 10, P10009,
[arXiv:1405.6569](#). [doi:10.1088/1748-0221/9/10/P10009](#).
- [18] H. Bethe, “Theory of the Passage of Fast Corpuscular Rays Through Matter”, *Annalen Phys.* **5** (1930) 325–400. [Annalen Phys.397,325(1930)].
[doi:10.1002/andp.19303970303](#).
- [19] “National Institute of Standards and Technology”.
<http://physics.nist.gov/cgi-bin/Star/compos.pl?mode=text&matno=014>.
Accessed: 2015-10-21.
- [20] Particle Data Group Collaboration, “Review of Particle Physics”, *Chin. Phys.* **C38** (2014) 090001. [doi:10.1088/1674-1137/38/9/090001](#).

- 477 [21] L. Landau, “On the energy loss of fast particles by ionization”, *J. Phys.(USSR)* **8**
478 (1944) 201–205.
- 479 [22] H. Bichsel, “Straggling in Thin Silicon Detectors”, *Rev. Mod. Phys.* **60** (1988)
480 663–699. doi:10.1103/RevModPhys.60.663.
- 481 [23] L. Quertenmont, “Search for Heavy Stable Charged Particles with the CMS
482 detector at the LHC”. PhD thesis, Louvain, U., 2010.
483 <https://inspirehep.net/record/1088192/files/openfile.pdf>.
- 484 [24] D. Kotlinski. personal communication.
- 485 [25] T. W. Anderson, “On the Distribution of the Two-Sample Cramr-von Mises
486 Criterion”, *The Annals of Mathematical Statistics* **33** (1962), no. 3, pp. 1148–1159.
- 487 [26] F. James, “Statistical methods in experimental physics”. 2006.
- 488 [27] CMS Collaboration, “Tracking and Vertexing Results from First Collisions”, *CMS*
489 *Physics Analysis Summary* **CMS-PAS-TRK-10-001** (2010).

